Integrative Biology, 2020, 00(00),1–16

doi: 10.1093/intbio/zyaa005
Original Article

ORIGINAL ARTICLE

Human brain microvascular endothelial cell pairs model tissue-level blood–brain barrier function

Blakely B. O'Connor[1,‡], Thomas Grevesse[1,†,‡], John F. Zimmerman[1], Herdeline Ann M. Ardoña[1], Jorge A. Jimenez[1], Dimitrios Bitounis[2], Philip Demokritou[2], and Kevin Kit Parker[1,*]

[1]Disease Biophysics Group, Wyss Institute for Biologically Inspired Engineering, Harvard John A. Paulson School of Engineering and Applied Sciences, Harvard University, Cambridge, MA 02138, USA, and [2]Center for Nanotechnology and Nanotoxicology, Department of Environmental Health, T. H. Chan School of Public Health, Harvard University, Boston, MA 02115, USA

*Corresponding author. E-mail: kkparker@seas.harvard.edu
†Present address: Department of Biology, Concordia University, 1455 Boulevard de Maisonneuve O, Montréal, QC H3G 1M8, Canada
‡Authors contributed equally.

Abstract

The blood–brain barrier plays a critical role in delivering oxygen and nutrients to the brain while preventing the transport of neurotoxins. Predicting the ability of potential therapeutics and neurotoxicants to modulate brain barrier function remains a challenge due to limited spatial resolution and geometric constraints offered by existing *in vitro* models. Using soft lithography to control the shape of microvascular tissues, we predicted blood–brain barrier permeability states based on structural changes in human brain endothelial cells. We quantified morphological differences in nuclear, junction, and cytoskeletal proteins that influence, or indicate, barrier permeability. We established a correlation between brain endothelial cell pair structure and permeability by treating cell pairs and tissues with known cytoskeleton-modulating agents, including a Rho activator, a Rho inhibitor, and a cyclic adenosine monophosphate analog. Using this approach, we found that high-permeability cell pairs showed nuclear elongation, loss of junction proteins, and increased actin stress fiber formation, which were indicative of increased contractility. We measured traction forces generated by high- and low-permeability pairs, finding that higher stress at the intercellular junction contributes to barrier leakiness. We further tested the applicability of this platform to predict modulations in brain endothelial permeability by exposing cell pairs to engineered nanomaterials, including gold, silver–silica, and cerium oxide nanoparticles, thereby uncovering new insights into the mechanism of nanoparticle-mediated barrier disruption. Overall, we confirm the utility of this platform to assess the multiscale impact of pharmacological agents or environmental toxicants on blood–brain barrier integrity.

Key words: blood–brain barrier; endothelial cells; micropatterning; nanotoxicology

Received October 29, 2019; **revised** December 23, 2019; **editorial decision** ; **accepted** January 5, 2020

INSIGHT

Current models of the blood–brain barrier provide limited mechanistic insights into the ability of therapeutics and toxins to impact barrier permeability. Here, we implement a minimalist approach to probe the contribution of endothelial cell interactions on blood–brain barrier function. Using brain microvascular cells patterned on geometrically defined fibronectin islands, we identify structural metrics that correlate with tissue-level endothelial barrier permeability. We found that increased stress formation at the cell–cell junction, accompanied by actin rearrangement and decreased junction protein expression, contributed to barrier leakiness in endothelial tissues. Using cell pairs as an alternative to traditional barrier screening platforms, we found that certain engineered nanomaterials, such as silver nanoparticles and nanoceria, can modulate brain endothelial structure and permeability.

INTRODUCTION

The blood–brain barrier serves as a boundary between the circulatory system and the brain that maintains cerebral homeostasis by protecting the brain from neurotoxins and pathogens while still supplying the brain parenchyma with oxygen and nutrients. The blood–brain barrier's ability to maintain homeostasis is largely dictated by the integrity of endothelial cell junctions and basement membrane, where structural organization at the intercellular, cellular, and subcellular levels gives rise to functional tissues that dynamically regulate solute transport. Although the blood–brain barrier can serve as a highly selective membrane, barrier permeability can fluctuate during development or disease. For example, vessels become more leaky during angiogenesis [1], inflammation [2], traumatic brain injury [3,4], and neurodegenerative diseases [5,6]. Unfortunately, predicting and understanding how bioactive reagents can modulate barrier function remain a challenge.

Understanding how changes in brain endothelial cell architecture contribute to blood–brain barrier function can provide insights into developing therapies to control its permeability while allowing us to predict how harmful toxins can infiltrate and disrupt the central nervous system. This is especially important for emerging technologies, such as engineered nanomaterials (ENMs), which have seen increased use as potential therapeutics and food additives but have yet to be excluded as possible environmental toxicants [7–9]. Three types of increasingly prominent ENMs are citrate-capped gold (AuNP), cerium dioxide (CeO_2), and silver-on-silica (Ag–SiO_2) nanoparticles. While these ENMs have been previously studied in terms of their potential pulmonary and cardiovascular toxicity upon inhalation as well as their translocation through the blood–air barrier [10–12], their biological effects at the blood–brain barrier remain largely unknown. Furthermore, while some ENMs can be directly transported across the blood–brain barrier, ENMs can also disrupt normal endothelial barrier function, leading to altered homeostasis and potentiating the transport of other neurologically active agents or pathogens [13].

Current models of blood–brain barrier integrity often focus on recreating multicellular interactions and complex tissue structures found in the neurovascular unit [14–16]. However, models that comprise multiple cell types, microfluidic connections, and complex manufacturing techniques are often lower throughput and not amenable to rapid screening of drug or toxicant response. Modifications in the morphology of individual cells have been shown to be good predictors of tissue-level structure and function [17]. Still, tissue-level models often lack the spatial resolution or architectural control needed to quantitatively determine cellular and subcellular responses, while heterogeneity in cell shape and contact geometries makes it difficult to normalize structural features across multiple cells. Alternatively, plate-based microfluidic models of the blood–brain barrier offer rapid assessment of tissue permeability as an end-point measurement [18], but such systems do not provide mechanistic insight into how tissue structure influences barrier integrity. To overcome these limitations, geometrically defined cell pairs and microtissues have emerged as tools to probe tissue behavior at the cellular level [19–21]. For example, cell pairs have been used to study endothelial cell cohort migration [22], cardiac myocyte coupling [23], and mechanical tugging of endothelial cells [24]. Such platforms that rely on scalable soft lithography are advantageous because they are amenable to multiplexing and provide an opportunity for higher-throughput screening of pharmacological agents. We recently developed a cell pair platform to screen the effects of ENMs on vascular endothelial cell structure and permeability [25]. Thus, we sought to expand upon this platform to generate a microtissue model of the blood–brain barrier and investigate the relationship between intracellular and intercellular structures in endothelial cell pairs and tissue permeability.

Here, we recreate the minimal tissue interaction in the blood–brain barrier—two cells on a geometrically confined extracellular matrix island—to predict changes in tissue permeability based on cellular morphology and junction formation. We generated pairs of human brain microvascular endothelial cells (HBMECs) using microcontact printing to deposit fibronectin in hexagonal patterns to allow for analysis of multiple samples from one coverslip. We treated cell pairs with pharmacological agents known to induce changes in cellular structure and tissue permeability to develop high- and low-permeability phenotypes. Using this platform, we showed distinct patterns of nuclear shape, junction formation, and cytoskeletal organization in high- and low-permeability conditions. We hypothesized that high-permeability tissues were a result of increased cytoskeletal tension, which was confirmed using traction force microscopy of cell pairs. Finally, to assess the ability of this platform to detect modifications of blood–brain barrier function under perturbation, we dosed endothelial cell pairs with ENMs (Au, Ag–SiO_2, and CeO_2) and compared their structural organization to predetermined high- and low-permeability states. This indicated that some ENMs are capable of modulating barrier function, which we confirmed using tissue-level barrier testing. Overall, our data suggests the utility of an endothelial cell pair platform to understand how changes in cellular architecture and tension translate to modulation in blood–brain barrier permeability. By adopting this approach, we hope to gain deeper mechanistic

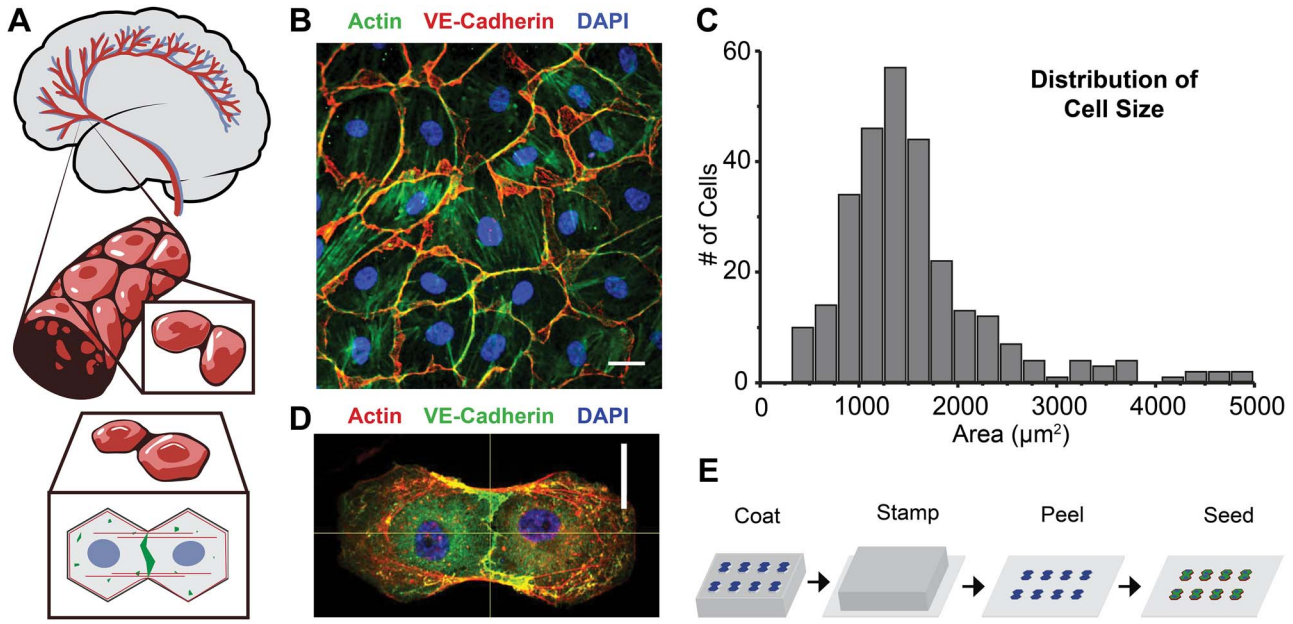

Figure 1. A minimalist model of the blood–brain barrier using brain microvascular endothelial cells. (A) Schematic of the cell pair concept. (B) Representative image of a brain endothelial tissue; scale bar = 20 μm; red, VE-cadherin; green, actin; blue, DAPI. (C) Histogram of individual cell areas measured in confluent tissues; n = 282 cells; (D) representative image of HBMEC cell pair; red, actin; green, VE-cadherin; blue, DAPI; scale bar = 20 μm. (E) Schematic of microcontact printing protocol.

insights into the impact of pharmacological agents and environmental toxicants on blood–brain barrier function.

RESULTS

Controlling cell pair architecture using soft lithography

The blood–brain barrier is primarily composed of confluent endothelial cells that form tight and adherens junctions between cells to regulate paracellular transport into and out of the brain [26]. Here, we used an established minimalist model [25] that incorporates two cells to recapitulate this important interaction in the blood–brain barrier (Fig. 1A). We used soft lithography to microcontact print islands of extracellular matrix and build geometrically controlled endothelial cell pairs, thereby limiting the variability of cell structure while enabling comparison between different test conditions [27]. To determine the appropriate size of each patterned cell, we measured the surface area of confluent HBMECs and used VE-cadherin immunostaining to delineate cell borders (Fig. 1B). We found that the average cell area was 1683 ± 863 μm^2 (mean ± SD; n = 262 measurements) (Fig. 1C). We then developed an island pattern that contained two adjacent hexagons with areas of 2500 μm^2 each, 5000 μm^2 total, selecting hexagonal cell islands as they are the most common polygonal shape observed in endothelial tissues [28]. Using polydimethylsiloxane (PDMS) stamps with bihexagonal features, we patterned PDMS-coated coverslips with fibronectin islands and seeded these substrates with HBMECs (Fig. 1D-E). Using this method, we confirmed high-fidelity printing of fibronectin islands and geometrical control of cell pair architecture, thereby constructing a minimalist model to probe the regulatory role of subcellular structures in blood–brain barrier integrity.

Structural metrics to evaluate brain endothelial cell pairs

To identify key structural features of the cell and cell–cell interface that contribute to blood–brain barrier function, we treated HBMEC cell pairs with pharmacological agents known to modulate endothelial structure and permeability. For each condition, cell pairs were cultured in growth media for 48 hours, replenishing media 24 hours after seeding (Fig. 2A). For drug treatment conditions, we dosed cell pairs with drugs that activate and inhibit the Rho pathway for 4 hours. Activation and inhibition of the Rho pathway are both known to induce barrier leakiness in endothelial culture [29]. We also dosed cell pairs with a cAMP analog, 8-(4-chlorophenylthio) adenosine 3′-5′-cyclic monophosphate, and a selective inhibitor of cAMP-specific phosphodiesterase for 24 hours, which has been shown to improve barrier function [30]. We then fixed and stained untreated and treated cell pairs to visualize the nucleus, cell–cell junctions, and cytoskeleton (Fig. 2B–E). To generate average composite images for each condition, cell pairs were aligned based on the geometry of the underlying fibronectin islands (Supplementary Figs S1 and S2). Finally, we quantified changes in nuclear morphology, junction area, and actin span to identify unique structural phenotypes that map to tissue permeability.

Nuclear morphology is intimately linked to cell shape and actin cytoskeleton organization and has been previously shown to play an important role in regulating endothelial function and vascular contractility [17,31]. As a result, we examined nuclear morphology as a metric of barrier permeability. To quantify nuclear shape and location within each pair, we measured nuclear eccentricity and the distance between nuclei (Fig. 2F, Supplementary Fig. S3). We expected to see nuclear elongation in cell pairs that were under increased cytoskeletal tension, i.e. Rho activation, with decreased internuclear distance as

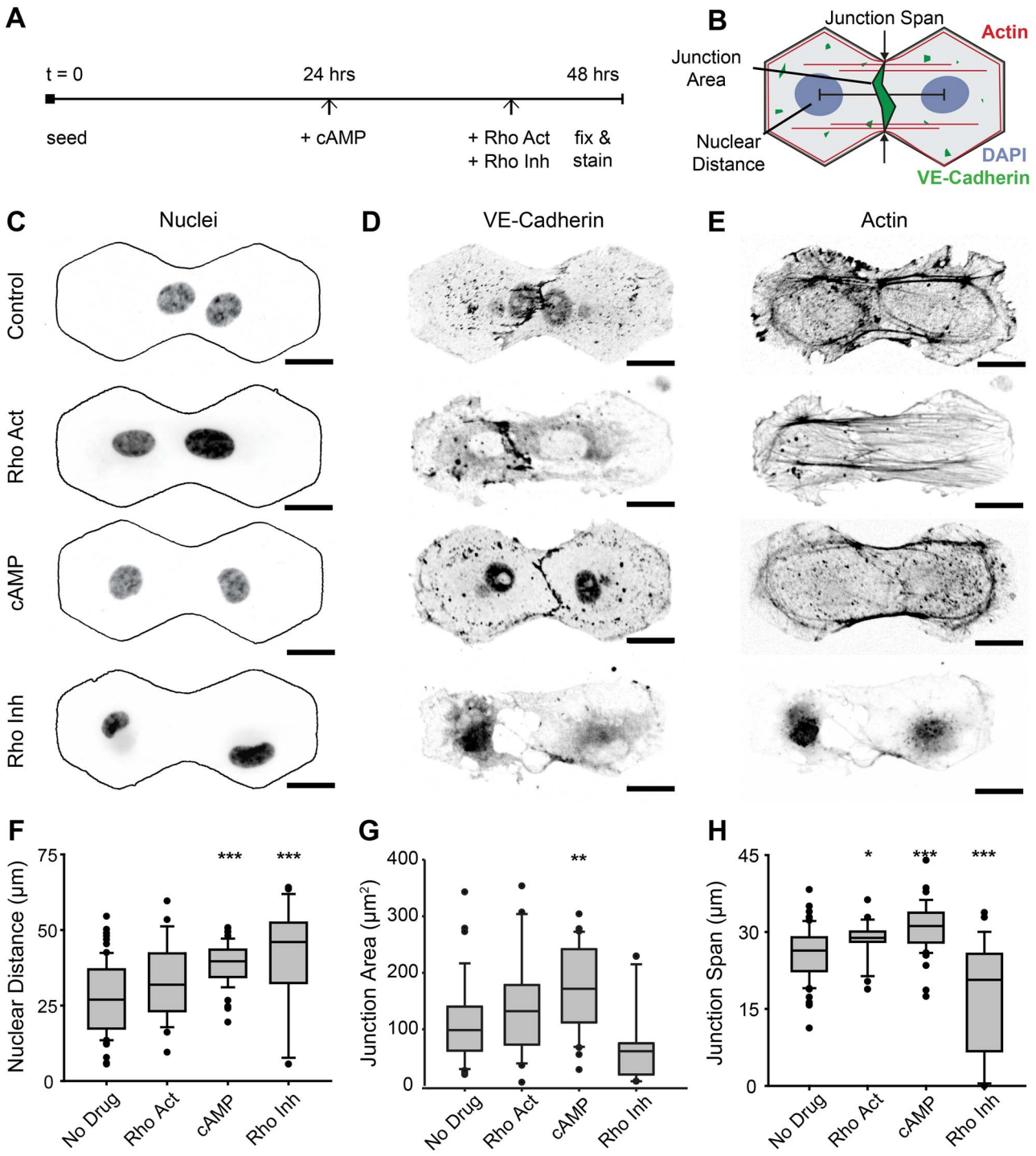

Figure 2. Assessment of nuclear, cytoskeletal, and junction protein morphology and localization in cell pairs. (A) Experimental timeline of culture and dosing procedure. (B) Schematic of structural components evaluated; representative fluorescent images of untreated cell pairs and cell pairs dosed with Rho activator, cAMP, and Rho inhibitor stained for (C) nuclei, (D) VE-cadherin, and (E) actin. (F–H) Quantification of structural metrics; (F) distance between nuclear centroids; (G) average VE-cadherin junction area; (H) length of actin spanning the cell pair junction; $n \geq 24$ cell pairs per condition; box = median ± quartiles; whiskers = 5 and 95 percentiles; $^{***}P < 0.001$, $^{**}P < 0.01$, and $^{*}P < 0.05$ using Holm–Sidak method for multiple comparisons versus control.

the cytoskeleton draws nuclei toward the junction. However, we observed nuclear elongation in both Rho activation and inhibition (6 and 10%, respectively). Upon closer inspection, Rho inhibition caused a 40% decrease in nuclear area along with a 41% increase in nuclear separation, indicating cell detachment or apoptosis as a potential cause of nuclear deformation rather than increased cytoskeletal tension (Supplementary Fig. S3B and C). We expected and observed the opposite trend for nuclear shape and localization in cAMP-treated cell pairs. Nuclei in cAMP-treated pairs were rounder and further apart,

suggesting either cytoskeletal rearrangement or relaxation that relieved tension across the nucleus and potentially at cell–cell junctions (Supplementary Fig. S2A). These differences in nuclear eccentricity and area, as well as internuclear distance, provide valuable metrics to evaluate cell shape and health that influence barrier permeability.

To quantify structural integrity of endothelial junctions in each cell pair, we measured the area of VE-cadherin in the central region of each cell pair island. VE-cadherin is the primary adhesion molecule that modulates attachment between brain endothelial cells and therefore regulates barrier permeability [32,33]. We expected to see an increase in cadherin area in cAMP-treated pairs, as cAMP stabilizes junction adhesion to the cytoskeleton [30]. cAMP-treated pairs showed a 55% increase in VE-cadherin area at the cell–cell junction (Fig. 2G), as well as increased cadherin expression throughout the cell pairs (Supplementary Fig. S2B). Cell pairs treated with Rho activator showed little change in junction area, while those treated with Rho inhibitor exhibited a more heterogeneous response. Some Rho-inhibited pairs had intact or unchanged cell–cell junctions, while others had diminished junction staining between cells with severely retracted cell bodies (Fig. 2D). Differential junction size as measured by the area of cadherin staining at the cell–cell junction provides a promising metric of barrier integrity to infer paracellular permeability.

The organization of the actin cytoskeleton contributes to nuclear morphology and junction size, as actin filaments bind to adhesion proteins at cell–cell and cell-matrix contacts and regulate cell architecture and barrier function [34]. To observe actin cytoskeleton in the cell pairs, we stained for f-actin filaments using a phalloidin stain (Fig. 2E). Untreated control cell pairs showed a variety of actin polymerization patterns, with both stress fibers that span the cell and cortical rings that localize to the cell border. We expected to see differences in actin organization in each treatment group, shifting either toward more stress fiber generation or cortical actin stabilization. As expected, Rho activation induced a hyper-polymerization of stress fibers that span the cell body, while cAMP treatment reduced stress fiber formation and stabilized cortical rings. Rho inhibition induced a loss of both stress fibers and cortical actin, with actin stain localizing to the perinuclear region of collapsed cell bodies. We averaged the distribution of actin across the vertical and horizontal axes of each cell pair condition and confirmed increased cortical actin in cAMP-treated, stress fiber formation in untreated and Rho-activated pairs and reduced actin content in Rho-inhibited pairs (Supplementary Fig. S4). Interestingly, we also observed differences in width of actin staining across the cell–cell junction or center of the vertical axis, despite constraining geometries with fibronectin islands. This junction span increased by 20% in cAMP-treated pairs, extending past the central width of the patterned island, while Rho inhibitor-treated cell pairs were 38% thinner at the junction (Fig. 2H). By analyzing actin organization within each cell pair, we gain insight into the cytoskeletal integrity of each cell, which is suggestive of potential to form stable barriers.

Collectively, these quantitative metrics capture key features of intercellular and subcellular structures in our cell pair platform that have been shown to contribute to brain endothelial tissue homeostasis and barrier permeability. Next, we measured the effects of each pharmacological agent on barrier permeability and compared these results to the structural phenotypes observed in each group at the cell pair level. In doing so, we sought to identify metrics that correlate directly to barrier permeability and to assess the ability of our platform to serve as a predictive tool for screening pharmacological agents that perturb barrier function.

Mapping cell pair structural metrics to tissue-level structure and permeability

To evaluate the barrier function of endothelial tissues with and without pharmacological agents, we measured the transport of 1.2-kDa fluorescent particles during static diffusion across cultured endothelial barriers. In this experiment, HBMECs were grown to confluence in Transwell culture dishes for 3–4 days. Confluent tissues were treated with cAMP for 24 hours or with a Rho activator or inhibitor for 4 hours (Fig. 3A). To measure permeability, fluorescent tracers were added to media in the top insert and were allowed to diffuse across the barriers for 30 minutes. Fluorescent intensities of the media collected from the top insert and bottom well were used to calculate permeability coefficients before and after exposure. These coefficients were then normalized to the untreated condition to find the percent change in permeability (Fig. 3B). HBMECs treated with both Rho activator and inhibitor showed an increase in permeability coefficients and barrier leakiness (~100 and 200% increases, respectively). Conversely, treatment with cAMP decreased permeability and increased barrier function by ~44%. Collectively, these conditions represent a range of endothelial tissue permeabilities, allowing us to map their respective cellular structures to barrier function or leakiness.

To determine the cellular characteristics that contribute most to tissue function, we performed principal component (PC) analysis (PCA), generating biplots of each condition and the measured variables (Fig. 3C). The first two PCs account for 90.4% of the variation observed in the data. This analysis showed that cAMP and Rho-inhibited pairs were distinct from each other and untreated cell pairs, but Rho-activated pairs were similar to untreated controls with respect to the PCs. Analysis of cell pair characteristics show that nuclear eccentricity is positively correlated with barrier permeability such that nuclear elongation is associated with more barrier leakiness. Furthermore, size of the cell–cell interface, including junction span and area, was negatively correlated with change in barrier permeability; reduction of junction area and span is mapped to more barrier leakiness. Taken together, this analysis allows us to establish a structural phenotype for chemically induced high- and low-permeability endothelial tissues that can be used to probe underlying mechanisms of barrier function and screen potentially bioactive reagents in a high-throughput manner.

Based on these observations, we sought to further probe the contribution of cell and tissue structure in the resulting high- and low-permeability states. We selected cAMP-treated tissues as representative for the low-permeability condition and untreated tissues in normal growth medium as the high-permeability condition. Then we further tested their functional phenotypes by evaluating barrier permeability over extended culture times, observing a sustained 40% improvement in barrier function in the cAMP-treated condition over the course of 3 weeks (Fig. 3D). To assess the tissue organization of high- and low-permeability states, we stained confluent endothelial tissues for the actin cytoskeleton and VE-cadherin (Fig. 3E). Similar to the trends observed in cell pairs, we observed more cortical actin rings in low-permeability tissues and more stress fibers in high-permeability tissues. Staining for junction proteins showed that low-permeability tissues had more VE-cadherin localization to the cell–cell junction compared to more diffuse staining in the high-permeability case. Western blot analysis of additional

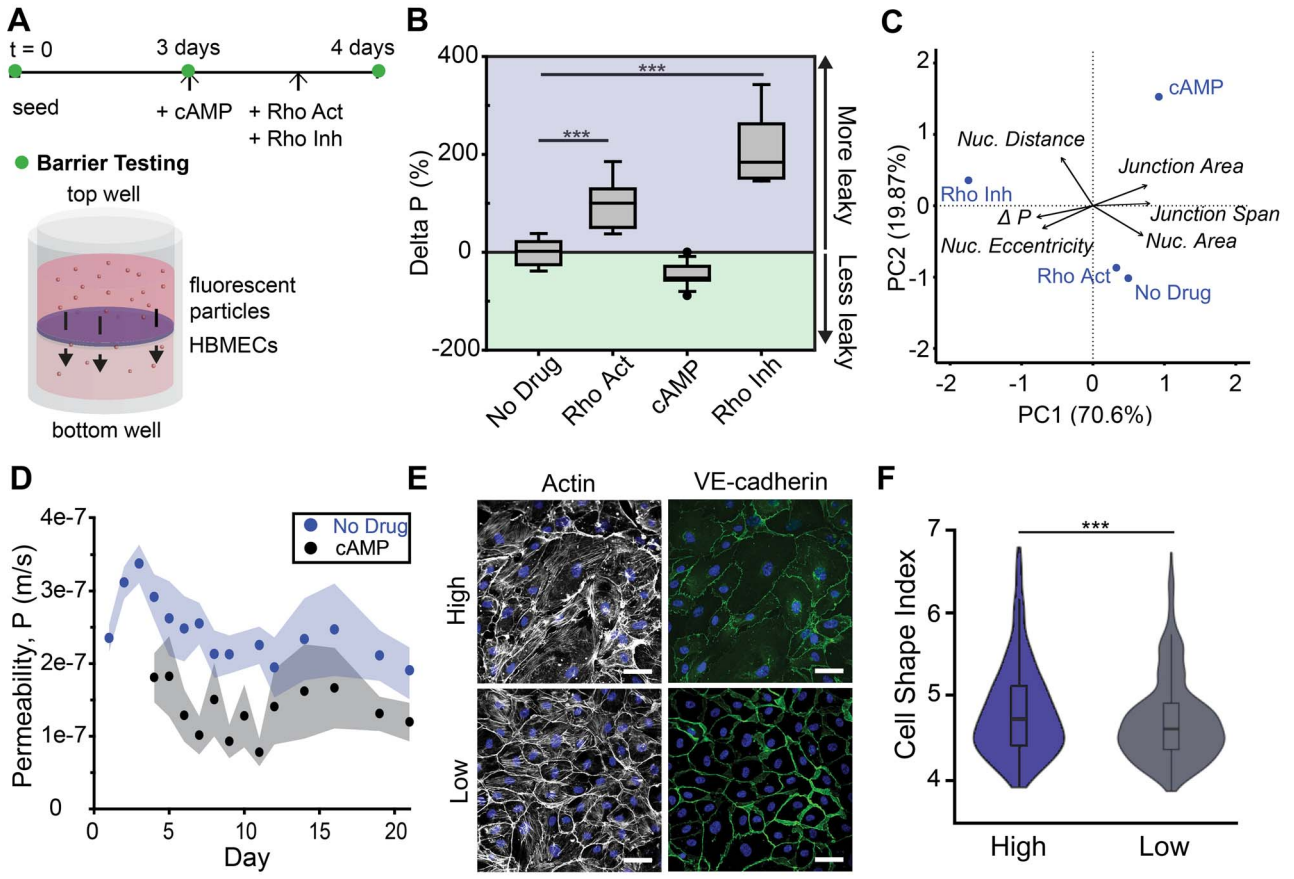

Figure 3. Mapping structural metrics to barrier function. (A) Experimental timeline of barrier testing protocol, which schematic of fluorescent tracer transport across a Transwell barrier tissue. (B) Quantification of HBMEC barrier function in untreated and treated tissues, reported as percent change in permeability coefficients, *P*, or 1.2-kDa tracers relative to untreated controls; $n = 7+$ wells per condition; box = median ± quartiles; whiskers = 5 and 95 percentiles; $^{***}P < 0.001$ for Holm–Sidak methods for multiple comparisons versus control. (C) PCA biplot containing average projection for each condition and impact of each measured variable. (D) Extended barrier experiments for untreated and cAMP-treated tissues, reported as permeability coefficients of 1.2-kDa tracers measured every 2 days over 21 days in culture; $n = 12$ wells per condition; mean ± standard deviation. (E) Immunohistochemistry of untreated and cAMP-treated tissues at day 10. blue, DAPI; white, actin; green, VE-cadherin; scale bar = 50 μm. (F) Cell shape index for high- and low-permeability tissues; $n \geq 300$ cells per condition; $^{***}P < 0.001$ for Mann–Whitney rank sum test.

junction proteins confirmed that low-permeability tissues expressed almost twice as much VE-cadherin (Supplementary Fig. S5). Finally, we noted each condition showed unique cellular organization within the tissues. Low-permeability tissues had more rounded or cobblestone-like cell shape, whereas high-permeability tissues had more elongated cells that appeared more motile.

To quantify structural differences in the confluent tissues, we measured differences in cell area and cell shape using thresholded images of VE-cadherin to identify cell borders (Supplementary Fig. S6). Reports have shown that epithelial tissues undergo a morphological transition from a fluid-like state to a solid, or jammed, state when a major phenotypic switch occurs, such as during development or the transition from a healthy to a pathological state [35]. Jammed cells are more round and non-motile relative to each other (low cell shape index), while unjammed cells adopt a more elongated shape as they flow or migrate through the tissue (high cell shape index) [36]. Both high- and low-permeability tissues had a cell shape index above a predefined jamming transition of 3.81 (normal = 4.86 ± 0.62; cAMP = 4.71 ± 0.47; mean ± SD) indicating that neither of the two tissues are completely jammed (Fig. 3F). However, we observed a lower cell shape index in low-permeability tissues, trending toward the liquid-to-jammed transition. This suggests that low-permeability tissues are relatively stable compared to the high-permeability tissues and that the cellular organization within tissues contributes to barrier permeability.

The role of tension in high- and low-permeability cell pairs

Based on the structural observations in high- and low-permeability cell pairs and tissues, we hypothesized that tension across the cell–cell junction may contribute to the barrier leakiness. To understand the molecular contributors associated with increased tension in our cell pairs, we examined both focal adhesion complexes and myosin light chain expression, which work concertedly with actin to regulate force transmission, cell motility, and barrier permeability (Fig. 4) [37–40]. Vinculin focal adhesion staining was localized to the cell periphery in both high- and low-permeability cell pairs (Fig. 4A, Supplementary Fig. S7A). Focal adhesions in high-permeability pairs were elongated and aligned toward the cell–cell junction, whereas focal adhesions in low-permeability cell pairs were more punctate. We also observed an increase in myosin light chain that was colocalized with actin stress fibers in high-permeability cell pairs (Fig. 4B, Supplementary Fig. S7B), indicating activation of the contractile apparatus. Importantly,

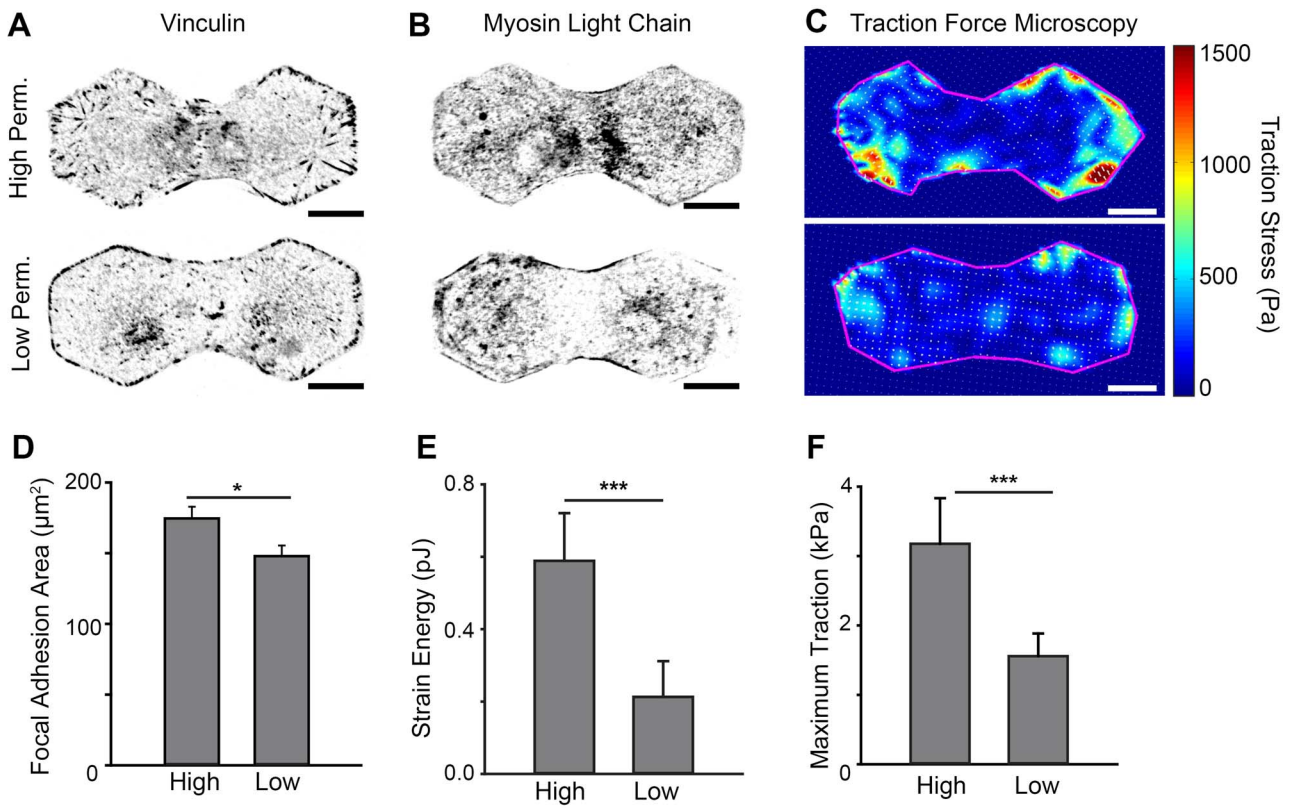

Figure 4. Using cell pair platform to evaluate differences in contractile state of high- and low-permeability cell pairs. (A) Representative fluorescent images of vinculin staining in high- and low-permeability cell pairs. (B) Representative fluorescent images of myosin light chain staining in high- and low-permeability cell pairs. (C) Traction stress maps of high- and low-permeability cell pairs; scale bar = 20 μm. (D) Focal adhesion area excluding the nuclear area mask for high- and low-permeability cell pairs; $n \geq 14$; mean ± SEM. (E) Average strain energy of control and cAMP-treated cell pairs. (F) Maximum traction generated by each cell pair; $n \geq 17$; mean ± SEM; $^{*}P < 0.05$ and $^{***}P < 0.001$ for two-sample *t*-test.

similar expression patterns were observed in high- and low-permeability tissues (Supplementary S7C). Quantification of positive vinculin staining outside the nucleus showed increased focal adhesion formation in high-permeability pairs compared to low-permeability pairs (control = 175 ± 8 μm², cAMP = 148 ± 7 μm², mean ± SEM) (Fig. 4D). Taken together, increases in focal adhesion complexes and myosin light chain activation further suggested an increase in cell contractility and tension across the cell pair.

To evaluate the relationship between tissue permeability and intercellular tension, we performed traction force microscopy on cell pairs prepared on soft hydroxy-polyacrylamide (PAAm) hydrogels with embedded fluorescent beads (Young's modulus = 8.7 kPa). By measuring the displacement between the beads before and after trypsinization, we generated a map of traction stresses generated by cell pairs in the high- and low-permeability states. Typical maps for high- and low-permeability cell pairs show that stresses localized to the cell periphery, with high-permeability cell pairs generating more force than low-permeability pairs (Fig. 4C). The integration of the traction stresses over the surface area occupied by each cell pair also shows higher strain energies in high-permeability cell pairs (Fig. 4E). On average, high-permeability pairs generated larger traction stresses and more strain energy (3.2 ± 0.65 kPa and 0.59 ± 0.13 pJ, mean ± SEM, $n = 17$), compared to low-permeability pairs (1.6 ± 0.33 kPa and 0.21 ± 0.10 pJ, mean ± SEM, $n = 26$) (Fig. 4E and F). These results suggest that high-permeability cell pairs are more contractile than low-permeability cell pairs, indicating that intercellular tension plays an important role in regulating brain endothelial barrier function.

Screening brain endothelial cell pair response to ENM exposure

To test the ability of our platform to detect organizational alterations in response to potential toxicants, we exposed brain endothelial tissues and cell pairs to a variety of ENMs. ENMs are increasingly used in commercial products and biological therapies [41], but their potential to induce endothelial toxicity or manipulate blood–brain barrier permeability is not well understood. As a result, there is still a need for improved *in vitro* methods to study the toxicity of these materials, making them ideal candidates to evaluate using this cell pair system. We selected 18-nm AuNP as an inert control [42], 10% 7-nm silver supported on 10-nm silica (Ag–SiO_2) as an engineered composite known to disrupt cell integrity [43], and 10-nm CeO_2 as a test nanoparticle that is currently being studied as a potential treatment for neurodegenerative disorders [44]. We evaluated the structural phenotype of both cell pairs and confluent tissues exposed to these ENMs at a concentration of 10 μg/mL dispersed in cAMP media, a concentration at the lower end of typical metal and metal oxide nanoparticle toxicology studies [45, 46], and compared them to cAMP-treated cell pairs as a control. Finally, we evaluated our minimalist predictive model

by measuring the permeability coefficients of endothelial monolayers that underwent the same ENM exposure conditions as the cell pairs.

To assess potential disruptions in subcellular organization, we measured nuclear morphology and localization, cadherin junction area, and actin organization in cAMP-treated controls and ENM-exposed cell pairs (Fig. 5A–C and Supplementary Fig. S8). Composite images of the nuclei show minimal differences between ENM-treated pairs and the controls (Fig. 5A), and the quantified nuclear distances were also similar (Supplementary Fig. S8B). Composite images of VE-cadherin composites show differences in expression in exposures groups. Ag–SiO_2-treated pairs had reduced cadherin staining overall, while CeO_2-treated pairs showed an increase in nuclear cadherin intensity (Fig. 5B, Supplementary Fig. S8C). The quantification of VE-cadherin area shows a significant decrease in junction size for Ag–SiO_2-treated pairs but no change in junction span (Supplementary Fig. S8D and E). Finally, actin composites show some remodeling in Ag–SiO_2- and CeO_2-treated cell pairs (Fig. 5C), where the ratio of cortical actin intensity to centralized actin intensity increased in CeO_2-treated pairs (Supplementary Fig. S8F). One explanation for the variation in structural changes observed in Ag–SiO_2-treated and CeO_2-treated cell pairs is differences in oxidative stress within the cell. Silver nanoparticles readily generate reactive oxygen species [47], while nanoceria can act as radical-mediated antioxidant (Supplementary Fig. S9A–C). In Ag–SiO_2-treated HBMECs, we found that oxidative stress doubled when compared to cAMP-treated controls, while CeO_2-treated HBMECs remained unchanged. Importantly, these differences in reactive oxygen species generation and subsequent cellular oxidative stress can lead to impaired actin polymerization *in vitro* [48].

We also compared structural changes in confluent tissues treated with ENMs (Supplementary Fig. S8A). In confluent tissues, the cell shape index decreased in both AuNP- and Ag–SiO_2-treated tissues, suggesting a decrease in cell motility and an increase in tissue jamming (Supplementary Fig. S8H). However, Ag–SiO_2-treated samples also showed a modest decrease in average cell area (13% reduction compared to cAMP-treated) (Supplementary Fig. S8I). To test if this was a result of cell retraction due to cell death, the mitochondrial reductase activity of cells treated with nanoparticles was measured using a colorimetric assay (Supplementary Fig. S9D). ENM-treated samples displayed similar activity as untreated controls, indicating that cell proliferation and viability were unchanged. Together, the structural characteristics at the pair and tissue level predict more barrier leakiness in Ag–SiO_2-treated tissues and potential barrier improvement in CeO_2-treated tissues.

Finally, we evaluated the barrier function of HBMECs treated with AuNP, Ag–SiO_2, and CeO_2 (Fig. 5D) using the permeability coefficient of a 1.2-kDa fluorescent tracer. We observed 238% increase in permeability for Ag–SiO_2-treated tissues and a 22% decrease in permeability for CeO_2-treated tissues compared to controls. These changes in tissue function map to the combined structural metrics we observed at both the cell and tissue level. To quantitatively compare the similarity between ENM-treated and control tissues, we calculated a similarity index based on Hellinger distances (Fig. 5E) as previously used to assess the outcome of stem cell therapies of myocardial infarction [49], wound healing efficacy [50,51], and ENM cytotoxicity [25]. For this index, a score of 100 indicates identical distributions and a score of 0 indicates no similarity. The combined score for AuNP-treated cells and tissues was 98.4, which is very similar to untreated controls. Both Ag–SiO_2- and CeO2-treated groups showed a decrease in similarity, with scores of 85.2 and 89.2, respectively. We also repeated the PC analysis using the nanoparticle-treated groups and found that junction span and junction area were similarly correlated with barrier permeability, while nuclear eccentricity was less correlated than in the previous pharmacological studies (Supplementary Fig. S8G). In summary, we found that CeO_2 and Ag–SiO_2 nanoparticles induced mild to moderate changes in brain endothelial cell pair structure that map to similar differences in barrier permeability.

DISCUSSION

In this study, we evaluated the response of the blood–brain barrier to drug and toxicant exposure by relating the structural changes in geometrically confined brain endothelial cell pairs to monolayer tissue permeability. We identified structural characteristics of HBMEC cell pairs and tissues treated with a variety of pharmacological agents that influence cell structure and tissue permeability. We investigated the contribution of cellular tension in regulating barrier function by performing traction force microscopy of high- and low-permeability cell pairs on soft deformable substrates. Finally, we assessed the structural and functional impact of ENM exposure on HBMEC cell pairs and tissues, further demonstrating the utility of this cell pair model to screen and predict the effects of bioactive agents on brain endothelial function.

Using pharmacological agents that modulate the cytoskeleton and endothelial barrier function, we found that HBMEC tissue permeability is regulated by the structure of intra- and intercellular components that coordinate tension within and between cells. We suggest that one mechanism of barrier disruption is a result of increased cellular tension and associated cytoskeletal remodeling, which leads to a decrease in cell–cell junction integrity and increase in barrier permeability (Fig. 6). Previous studies have shown that mechanical forces on the cell can actively deform the nucleus via the cytoskeleton, where nuclear elongation occurs concomitantly with actin stress fiber formation [52,53]. Similarly, here we demonstrated that high-permeability cell pairs had more elongated nuclei, reduced internuclear distance, and an increase in actin stress fiber formation. In addition to this cytoskeletal remodeling, high-permeability cell pairs showed activation of contractile actin–myosin machinery and reinforcement of focal adhesions at the cell-matrix interface, suggestive of increased cytoskeletal tension. Traction force microscopy of cell pairs confirmed increased tension in high-permeability cell pairs, which translates to increased stress at the cell–cell junction. We have previously shown that coordinated remodeling of cell-matrix and cell–cell adhesions is necessary to balance forces between coupled cardiac myocytes and their underlying matrix in order to achieve structural and electro-mechanical coupling [23,54]. In the brain microvascular cell pairs presented here, the absence of cooperative remodeling of cell–cell adhesions to compensate for additional stress at the junction led to weakened intercellular junctions and barrier leakiness. Our experiments suggest that lower permeability and lower traction cell pairs have larger cadherin junctions than high-permeability pairs, which is consistent with previous reports that indicate intracellular cAMP stabilizes VE-cadherin–mediated adhesions between cells and cortical actin that improves endothelial barrier function [30]. Additionally, we observed adherens junction assembly and disassembly in HBMECs that was consistent with the remodeling previously reported in pulmonary artery endothelial cells in high and low

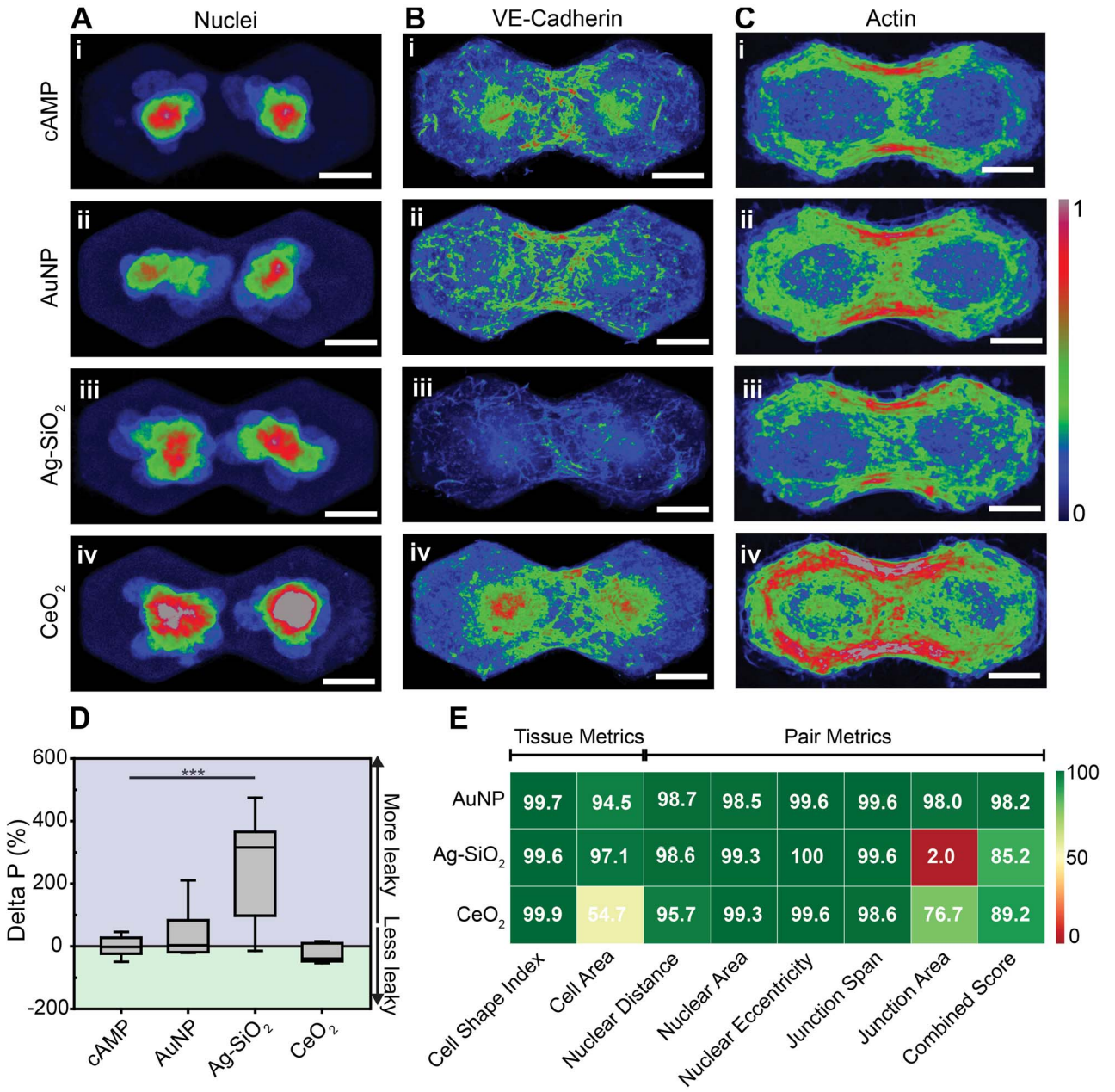

Figure 5. Structural and functional response of brain endothelial cell pairs and tissues to ENM exposure. HBMEC cells were cultured in cAMP media and exposed to gold nanoparticles (AuNP); silver nanoparticles suspended in nano-silica (Ag–SiO_2), and nanoceria (CeO_2) for 24 hours. (A–C) Composite images of untreated and ENM-treated pairs stained for nuclear, junction, and cytoskeletal proteins; pixel intensities normalized per stain on a scale of 0 to 1; scale bar = 20 μm. (D) HBMEC barrier function in response to ENM exposure; $n = 8$ samples per condition; mean ± SEM; ***$P < 0.001$ for Holm–Sidak test for multiple comparisons versus control. (E) Similarity index map of structural metrics measured in HBMEC tissues and cell pairs, comparing characteristics of ENM-treated conditions to cAMP-treated controls. The similarity index applies a modified Hellinger distance formula to compare the probability distributions of each measurement, where 0 represents complete dissimilarity and 100 represents identical distributions.

stress regimes [24]. Taken together, these results suggest an optimal balance of inter- and intracellular stresses that regulate vascular permeability.

When examining the structural metrics in HBMEC cell pairs exposed to ENMs, we were able to detect intracellular and intercellular changes that mapped to differences in tissue-level function. In our negative nanoparticle treatment control, AuNP-treated cell pairs showed minimal disruptions in brain endothelial cell morphology and permeability, which was consistent with previous experiments in HBMECs [55]. In our positive nanoparticle treatment control, Ag–SiO_2-treated pairs showed severe disruption of VE-cadherin junction expression, but only minimal changes were observed in cytoskeletal organization. While certain nanoparticles can induce actin rearrangement and barrier dysfunction like the tension-mediated mechanism described above [56], our results suggest that Ag–SiO_2 particles reduced barrier permeability through a mechanism independent of cellular tension (Fig. 6). An alternative explanation for Ag–SiO_2-mediated barrier disruption could be direct interference of cell–cell junctions, as select metal nanoparticles can interfere with homophilic interactions between VE-cadherin adhesions [57].

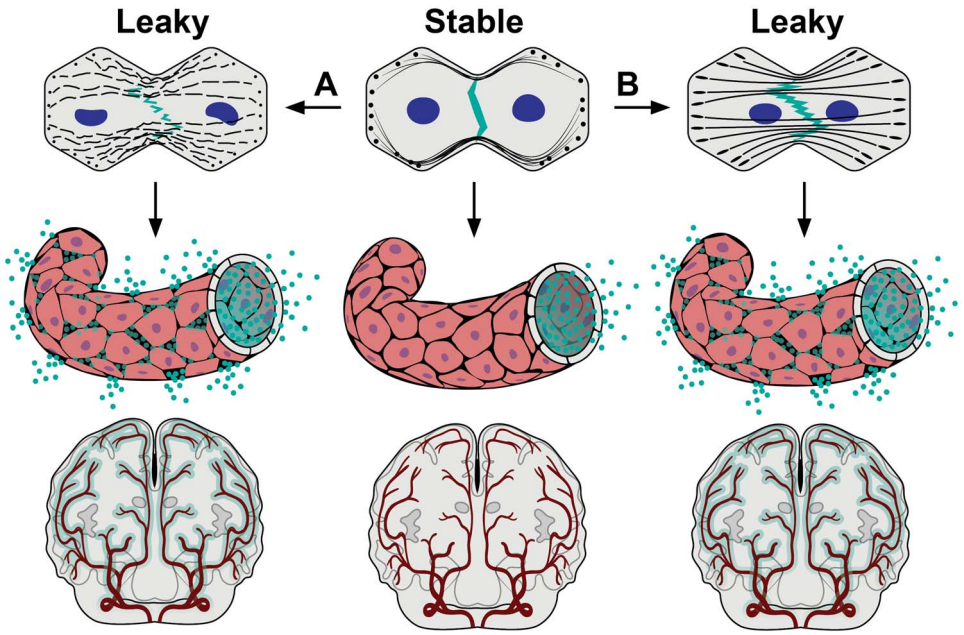

Figure 6. Summary of structural and functional changes observed in stable and leaky HBMEC tissues (center panel). Relaxed cytoskeletal tension confers a more stable cellular phenotype—marked by round nuclei, punctate focal adhesions, and intact cortical actin—leading to stabilized cell–cell junctions and reduced barrier permeability in cAMP-treated brain endothelium. (A) Reduction of cytoskeletal and cadherin expression and cell retraction leads to destabilized cell–cell junctions, thereby reducing junction integrity and increasing barrier leakiness, such as in the case of Rho inhibition and Ag–SiO_2 exposure. (B) Increased cytoskeletal tension—marked by increase in traction forces, nuclear eccentricity, focal adhesion area, and stress fiber generation—leads to a decrease in cell–cell junction integrity and increase in barrier leakiness, as observed in Rho activation and untreated HBMECs.

In the test case of nanoceria exposure, we were interested to see if CeO_2 nanoparticles could improve HBMEC structure and function as it is currently being researched as a potential therapeutic for neurodegenerative diseases [58]. It is hypothesized that the antioxidative capacity of CeO_2 reduces cellular oxidative stress within the tissue, thereby improving barrier function. In our experiments, CeO_2-treated pairs and tissues showed slight improvements in barrier function and increase in actin and VE-cadherin staining. Based on the structural and functional metrics measured, CeO_2-treated cell pairs had lower similarity indexes like Ag–SiO_2-disrupted cell pairs when compared to cAMP-treated controls. This is because our model assumes that any deviation from the cAMP-treated control state represents disruption to homeostasis, independent of whether the outcome is positive or negative. While this is an acceptable metric for determining toxicant risk, when determining drug efficacy intending to improve barrier function, it may be preferable to modify the index to signify whether a test agent improves or disrupts the function of the cells. Nevertheless, these findings demonstrate the utility of this minimalist model to detect changes in blood–brain barrier function using structural features of cell pairs.

In conclusion, we studied inter- and intracellular structures that manipulate blood–brain barrier permeability in response to chemical or toxicant exposure. Specifically, we used a micropatterning approach to recapitulate cell–cell interactions in the blood–brain barrier and identified key structural metrics involved in cellular remodeling as the cells transition from a high- to a low-permeability state. We observed changes in nuclear morphology, junction formation, and cytoskeletal organization that suggest brain endothelial barrier permeability is regulated in part by the contractility and tension between the junctions of adjacent cells. Finally, using the pair model, we detected changes in endothelial cell morphology and junction formation in response to ENM exposure, which mapped to alterations in barrier function at the tissue scale. Together, these findings shed light on the role of cellular tension in mediating brain endothelial permeability using a cell pair model. As a result, this platform can provide a path forward for higher-throughput preclinical research, disease modeling, or environmental exposure toxicity studies.

METHODS

PDMS substrate preparation

Glass coverslips were cleaned by sonicating in a 70% ethanol/water solution for 15 minutes. PDMS (Sylgard-184, Dow Corning, MI, USA) was mixed at a 10:1 mass ratio of base and curing agent, degassed using a Thinky Mixer (Planetary Centrifugal Mixer AR-100, Thinky, CA, USA), and spin-coated on to coverslips (G3P8 Specialty Spin Coater; SCS Inc., IN, USA). PDMS-coated coverslips were cured overnight in a 65°C oven before use.

Hydroxy-polyacrylamide gel preparation

Hydroxy-polyacrylamide-coated coverslips were prepared as previously described [59]. Briefly, we mixed 400 µL of 40% acrylamide solution (BioRad, CA, USA), 250 µL of 2% *N*, *N*′-methylenebisacrylamide solution (Sigma, St Louis, MO, USA), 65 mg of *N*-hydroxyethylacrylamide (Sigma, St Louis, MO, USA) dissolved in 1 mL of 50 mM (4-(2-hydroxyethyl)-1-piperazineethanesulfonic acid (HEPES, Sigma, St Louis, MO, USA), and 3410 µL of HEPES 50-mM buffer. The mixture was degassed for at least 30 minutes under vacuum. About 30 µL of 0.2-µm red fluorescent microbeads (ThermoFisher Scientific, Waltham, MA, USA) were dispersed in the mixture immediately before polymerization. The polymerization was initiated by

addition of 2.5 µL of *N, N,N′, N′*-tetramethylethylenediamine (TEMED, ThermoFisher Scientific, Waltham, MA, USA) and 25 µL of ammonium persulfate (100 mg mL-1 solution in ultrapure water, Sigma, St Louis, MO, USA). About 20 µL drops of polymerizing solution were sandwiched between an activated 18-mm-diameter glass coverslip, previously treated for 1 hour with 3-(-trimethoxysilyl)propyl methacrylate (Sigma, St Louis, MO, USA), and a 25-mm-diameter coverslip exposed to UV ozone for 7 minutes. The gels were polymerized for 30 minutes, and the two coverslips were separated under water using a flexible razor blade. Coverslips were rinsed in sterile water and stored in PBS until use.

Photo- and soft lithography

Polymer stamps were manufactured using standard photolithographic protocols, as previously described [60]. A photolithographic mask was designed with hexagonal cell pair features with a regular side length of 31 µm (Output City Bandon, OR, USA). Silicon wafers (76-mm diameter) were spin-coated with a layer of negative photoresist, SU-2002 (MicroChem Corporation, Westborough, MA, USA). After baking, coated silicon wafers were exposed to UV light through the photolithographic mask for 7–10 seconds. Subsequently, the regions not exposed to UV light were washed away using a development solution, and wafers were cured by baking at 180°C for 30 minutes. The etched wafer served as a negative template for manufacturing stamps, where PDMS was poured over the template, degassed, and allowed to cure overnight at 65°C. Cured PDMS was removed from the wafer and cut into rectangular stamps.

To direct cellular growth along the cell pair geometry, extracellular matrix proteins were microcontact-printed on PDMS and hydroxy-PA-treated coverslips using previously published methods [27,59]. Briefly, PDMS stamps were incubated with 50 µg mL^{-1} human fibronectin (BD Biosciences, Woburn, MA, USA) in sterile water for 1 hour. Excess fibronectin solution was removed from the stamp using compressed air, and the stamp was carefully applied to either the activated PDMS surface for 2 minutes or to the dried hydroxy-PAAm for 1 hour. After careful removal of the PDMS stamp, PDMS coverslips were incubated with 1% Pluronics F137 (BASF, Germany) for 5 minutes to prevent cell adhesion around the printed geometries. Both PDMS and hydroxy-PAAm coverslips were rinsed with PBS and stored hydrated until cell seeding.

HBMEC cell culture

Primary HBMECs (Cell Systems, Kirkland, WA, USA) were cultured in growth media consisting of Complete Classic Medium with 10% serum supplemented with CultureBoost and BaccOff (Cell Systems, Kirkland, WA, USA). Upon receipt, cells were thawed and expanded in T-75 culture flasks (Corning, Tewksbury, MA) treated with Cell Attachment Factor (Cell Systems, Kirkland, WA, USA) at 37°C for 30 minutes. For cell passage and seeding, cells were rinsed three times with warm, sterile PBS (ThermoFisher Scientific, Waltham, MA, USA) and dissociated using warm 0.05% Trypsin-EDTA (ThermoFisher Scientific, Waltham, MA, USA). Cells were neutralized in warm media and centrifuged at 200 g for 5 minutes. The subsequent cell pellet was resuspended in 1 mL culture medium, counted, and seeded at various densities depending on the experiment, ranging from 5000 to 10 000 cells cm^{-2}. Cells were used for experiments between passage 3 and 8.

Cell pair assay with cytoskeletal-modulating drugs and ENMs

Cell pair experiments with cytoskeletal-modulating drugs were performed over the course of 48 hours. Cells were initially seeded in growth media, and media were replenished after 24 hours. Drug treatments were added either 24 or 4 hours before fixation. To induced elevated intracellular cAMP, pairs were treated with 125 µM 8-(4-chlorphenylthio) adenosine 3′5′-cyclic monophosphate (8-CPT-cAMP) (ABCAM, Cambridge, MA) and 17.4 µM RO-20-1724, a selective inhibitor of cAMP-specific phosphodiesterase (Santa Cruz Biotechnology, Dallas, TX, USA) for 24 hours. For the activation and inhibition of the Rho pathway, 1 µM Rho activator II and 0.1 µM of Rho inhibitor I (Cytoskeleton Inc., Denver, CO) was added 4 hours prior to fixation. Cell pair experiments with ENMs took place over the course of 72 hours. Cells were seeded in growth media and treated with cAMP media after 24 hours. At 48 hours, ENMs were added to fresh cAMP media and incubated for an additional 24 hours prior to fixation on Day 3.

Immunohistochemistry

HBMECs were washed gently with 37°C PBS and fixed with warm 2% paraformaldehyde diluted in PBS (v/v, Electron Microscopy Sciences, PA, USA) for 15 minutes. HBMECs were then permeabilized with 0.05% Triton X-100 (v/v, Sigma, MO, USA) in PBS for 10 minutes at room temperature. Fixed samples were rinsed with PBS three times before incubating with a mixture of 5% bovine serum albumin (w/v, West Grove, PA, USA) for 30 minutes at room temperature. Samples were rinsed three times with PBS and incubated with 1:200 primary antibody dilutions for 45 minutes at 37°C. See Supplementary Table S1 for complete list of primary antibodies and sources. Samples were rinsed three times with PBS and incubated with a secondary antibody solution consisting of 1:200 dilutions of Alexa Fluor 488 or 546-conjugated goat anti-mouse or anti-rabbit IgG (H + L) cross-adsorbed secondary antibodies, DAPI, and Alexa Fluor 633 Phalloidin (ThermoFisher, CA, USA) for 90 minutes at 37°C. Samples were rinsed three times in PBS, dried, and mounted on glass slides with ProLong Gold Antifade Mountant (ThermoFisher, CA, USA). Fluorescence microscopy was performed using a scanning disc confocal microscope (Olympus, Waltham, MA, USA) using a 20x (UPLSAPO20X) objective at room temperature.

Quantitative analysis of cell pair structural parameters

Cell pair image analysis was performed using FIJI, a distribution of ImageJ. Prior to subcellular metric analysis, each cell pair was centered and aligned based on the location of the fibronectin pattern (Supplementary Fig. S1). Uniform background subtraction and auto-contrasting were applied across stacks of cell pairs before creating composite images that depict the average staining intensity for each protein of interest (Supplementary Fig. S2). Pixel intensities were mapped to a Rainbow lookup table, where gray depicts saturated pixels. Nuclear area, eccentricity, and location were measured using ‘analyze particles’. Nuclear distance was determined by calculating the distance between nuclear centroids in each cell pair (Supplementary Fig. S3). Actin distribution was measured by taking the average intensities at the cell–cell junction and across the entire length of the cell pair for vertical and horizontal distribution (Supplementary Fig. S4). Actin span across the junction was determined by measuring the maximum and minimum y-values of thresholded actin stain at

the cell junction. Average actin intensity inside the central region of each cell (0–15 μm from the center of each hexagon) and at the periphery (15 μm to pair mask border) was used to calculate a cortical actin ratio (peripheral intensity/central intensity). VE-cadherin area was determined by thresholding images and summing the total area of particles near the junction. Nuclear cadherin intensity was quantified by measuring the average VE-cadherin staining intensity within each nuclear mask. Similarly, vinculin area was determined using thresholded areas outside of the nucleus. Custom ImageJ macros used for image analysis are available from the authors upon request.

Barrier permeability assay

Transwells (12 well polycarbonate inserts, 0.4-μm pore size, Corning, Tewksbury, MA, USA) were exposed to UV ozone for 7 minutes and incubated with human fibronectin (BD Biosciences, Woburn, MA, USA) at 50 μg mL^{-1} for 2 hours at room temperature. The wells were rinsed three times with PBS. HBMECs were seeded at a density of 40 000 cells per well (~35 000 cells cm^{-2}) in normal growth medium. The medium was exchanged 24 hours after seeding and every 48 hours thereafter. Barrier permeability was evaluated by measuring transport of fluorescent molecules from the top insert to the bottom well. Fluorescent media was prepared by adding 1 μL mL^{-1} of 1 mg mL^{-1} Alexa Fluor 555 conjugated carboxylic acid in DMSO (ThermoFisher Scientific, Waltham, MA, USA) to cAMP media. About 500 μL of fluorescent media was added to the top insert, with 1500 μL of cAMP media in the bottom compartment. Samples were equilibrated for 30 minutes at 37°C before 200 μL samples from the top and bottom compartment were transferred to a 96-well plate. Fluorescent intensity was quantified using a plate reader (BioTek, Winooski, VT, USA), and permeability coefficients were calculated using the following equation:

$$P = \frac{C_B V}{C_T A t} \tag{1}$$

where C_B is the concentration in the bottom compartment, C_T is the concentration in the top insert, V is the volume of the bottom insert, A is the surface area of the Transwell insert, and t is the incubation time of the experiment. Permeability measurements were performed before cell seeding and before and after exposure for exposure assays and every day for extended culture experiments.

Cell shape index

Images of endothelial VE-cadherin and nuclear staining were processed to identify cell borders to delineate cell size and shape. Analysis was performed in ImageJ, where background subtraction filters and auto-contrast functions were applied. Cadherin stains were thresholded and skeletonized, and nuclei were used to identify the center of each cell (Supplementary Fig. S6). Skeletonized areas without a nucleus were excluded from calculations. Using ImageJ 'analyze particles', the area and perimeter of each cell were recorded and used to calculate a cell shape index that characterizes the jammed state of the tissue as previously defined [36]. The cell shape index is given by

$$I = \frac{p}{\sqrt{A}} \tag{2}$$

where p is the cell perimeter and A is the cell area. Jammed tissues approach a cell shape index of 3.72, the theoretical value for all pentagonal cells, while unjammed tissues have greater cell shape indices.

Protein isolation and western blot

Protein was isolated from HBMEC tissues by lysing cells at 4°C in radioimmunoprecipitation assay lysis buffer (Sigma-Aldrich, St Louis, MO, USA) plus Complete Mini (Roche, Indianapolis, IN, USA). A capillary-based Wes Simple Western system (ProteinSimple, San Jose, CA, USA) was used to quantify protein expression levels according to the manufacturer's protocol. In brief, 0.5-μg lysate samples were loaded into each capillary, and proteins were separated by size in the separation matrix. Target junction and adhesion proteins were identified with the following primary antibodies: PECAM-1, VE-cadherin, Claudin-5, Vinculin, and focal adhesion kinase. See Supplementary Table S1 for antibody sources. GAPDH was used as a loading control to normalize expression levels in each sample. The proteins were immunoprobed using mouse and rabbit secondary antibodies and chemiluminescent substrates provided by the manufacturer. Chemiluminescent signals were detected and quantified using Compass Software (ProteinSimple).

Traction force microscopy

Traction force microscopy was performed as previously described [61]. Briefly, HBMECs were seeded at a density of 6500 cells cm^{-2} on patterned hydroxy-pAAm gels embedded with fluorescent beads. Culture medium was exchanged with growth or cAMP media 24 hours after seeding, and experiments were performed on Day 3. Differential contrast images of the cell pairs and fluorescent images of suspended microbeads were taken before and after cell detachment using 0.05% Trypsin-EDTA (ThermoFisher Scientific, Waltham, MA, USA). Bead displacement between the two images was used to calculate a traction stress field using constrained Fourier transform traction cytometry in MATLAB [62]. To calculate the total strain energy, U, applied by the cell on the elastic substrate, we used the equation as described in McCain *et al.* [23]:

$$U = \frac{1}{2}\sum_n A_n \left(u_{x,n}T_{x,n} + u_{y,n}T_{y,n}\right), \tag{3}$$

where u_i and T_i are the displacement and traction forces vectors in the i-direction and A is the discretized unit surface area of the cell. To calculate the maximum traction force applied by the cell pair on the substrate, we compared the magnitudes of traction force vectors $\vec{T}_n$ applied on discretized surface A_n over all discretized cell surfaces, selected the highest and divided it by the discretized cell surface

$$T_{max} = \frac{T_{n,max}}{A_n}. \tag{4}$$

ENM synthesis

The ENMs used in our experiments were procured, synthesized, and characterized by Engineered Nanomaterials Resource and Coordination Core (ERCC) which is part of Nanotechnology Health Implications Research (NHIR) Consortium at Harvard T.H. Chan School of Public Health. Specifically, citrate-capped Au nanoparticles were synthesized according to a modified version of the Turkevich method optimized for increased control over particle size and size polydispersity. Details on the synthesis and characterization of pristine Au nanoparticles are presented by Dong *et al.* [63]. The synthesis of Ag–SiO_2 and CeO_2 was performed using flame spray pyrolysis using a procedure optimized for the synthesis of nanoparticles for toxicological research [64]. Details on the synthesis parameters

and characterization of the particles have been presented by Beltran *et al.* [43].

ENM dispersion and colloidal characterization

Following a previously reported dispersion protocols [65–67], the Ag–SiO_2 and CeO_2 colloidal suspensions were prepared at a concentration of 500 μg mL^{-1} by sonicating the ENMs dispersed in ultrapure, DNase/RNase free distilled water (Invitrogen, Carlsbad, CA). We used an ultrasonic processor/sonic dismembrator (FB-505, Fisher Scientific, USA) with an acoustic power of 2.51 J/s, calibrated according to a literature protocol [68]. As previously described [69], the sonication time for the Ag–SiO_2 and CeO_2 colloidal solutions depends on the critical delivered sonication energy (DSE_{cr}) predetermined for each ENM type (DSE_{cr}, Ag–SiO_2 = 480 J mL^{-1}; DSE_{cr}, CeO_2 = 630 J mL^{-1}). The 10-μg mL^{-1} working solutions used in ENM exposure experiments were prepared by diluting 500-μg mL^{-1} stock solutions in HBMEC culture medium. For AuNPs, the supplied colloidal solutions were concentrated to 1200 μg mL^{-1} by using ultracentrifugation at 13 000 RPM for 20 minutes at 4°C, which was then redispersed in DI H_2O, vortexed for 30 seconds, and then diluted to the final working concentrations with HBMEC culture media. The hydrodynamic diameter (dH) of ENMs in water of HBMEC suspension (Supplementary Fig. 10) was measured using dynamic light scattering (Malvern Nanosizer, Worcestershire, UK).

ENM cytotoxicity, oxidative stress, and reactivity testing

To measure the effect of ENMs on HBMEC viability, a commercially available 3-(4,5-dimethylthiazol-2-yl)-5-(3-carboxymethoxyphenyl)-2-(4-sulfophenyl)-2*H*-tetrazolium (MTS) assay kit (Abcam, MA, USA) was used to detect mitochondrial reductase activity. For this test, HBMECs were seeded on 96-well plates at a density of 1300 cells cm^{-2}. The absorbance of MTS-treated culture media at 490 nm was recorded using a plate reader (Synergy HT; BioTek, NJ, USA). The background signals at 650 and 490 nm from each ENM suspension in fresh culture media were subtracted from the recorded absorbance values. Percent mitochondrial reductase activity for each ENM treatment group was normalized to the control group. To measure the oxidative stress generated upon exposure to ENMs, a fluorogenic CellROX® green probe (Invitrogen; Carlsbad, CA) assay was performed. For this test, HBMECs were seeded on 24-well plates at a density of 2500 cells cm^{-2}. One group of cells was treated with 200 μM menadione (Sigma-Aldrich, St Louis, MO, USA) for 1 hour as a positive control for oxidative stress. After ENM and menadione treatment, cells were incubated in 5 μM CellROX® green and 20 ng mL^{-1} Hoechst stain (ThermoFisher Scientific, Waltham, MA, USA) for 30 minutes. Samples were rinsed with PBS, fixed in 4% PFA, and imaged immediately using an EVOS M7000 Imaging System (ThermoFisher Scientific, Waltham, MA, USA). CellROX intensity values were normalized to the number of Hoechst-positive cells and corrected for background fluorescent intensity of cells and ENMs without the CellROX. An Amplex Red hydrogen peroxide/peroxidase assay (Invitrogen, Carlsbad, CA) was used to test the oxidative capacity of the CeO_2 nanoparticles. CeO_2 nanoparticles were added to a solution of hydrogen peroxide containing the Amplex Red reagent, and fluorescent intensity between 530 and 590 nm was measured every 10 minutes. A standard curve was generated using serial dilutions of hydrogen peroxide, which was used to calculate final hydrogen peroxide concentrations in CeO_2 and blank solutions.

Similarity index calculations

The similarity index was used to compare the ENM-treated tissues and cell pairs versus unexposed, cAMP-treated controls. The index applies a modified Hellinger distance formula to compare the similarity between two probability distributions. The index is given by

$$\text{Score} = 100 \times \left[\sqrt{\frac{2\sigma_a\sigma_b}{\sigma_a^2+\sigma_b^2}}\, e^{-\frac{(\mu_a-\mu_b)^2}{4(\sigma_a^2+\sigma_b^2)}} \right], \quad (5)$$

where μ is the mean and σ is the standard deviation of each metric. The calculated index ranges from 0 to 100, where 0 indicates complete dissimilarity and 100 indicates identical distributions. Similarity indices were calculated for tissue metrics (cell area and cell shape index), cell pair metrics (nuclear area, nuclear eccentricity, nuclear distance, junction span, and junction area), and permeability. Combine scores were determined by averaging the evaluated parameters.

Statistical analysis

Statistical analysis was conducted using SigmaPlot (Systat Software, Inc., San Jose, CA); data were first tested with the Shapiro–Wilk test for normality and the Levene median test for equal variance. Two-sample *t*-test tests were conducted for normally distributed datasets. Alternatively, Mann–Whitney rank sum test was used for non-parametric analysis if samples did not meet normality and equal variance assumptions. For multiple comparisons to control samples, such as in pharmacological and ENM exposure studies, Holm–Sidak method was used. PCA was performed using custom-made code in R. The data was first standardized, and the PCA was run on the standardized dataset using the Vegan package in R.

SUPPLEMENTARY DATA

Supplementary data is available at *INTBIO Journal* online.

CONFLICTS OF INTEREST

There are no conflicts of interest to declare.

FUNDING

This work was supported by the Harvard John. A. Paulson School of Engineering and Applied Sciences; the Wyss Institute for Biologically Inspired Engineering at Harvard University; the National Institute of Environmental Health Sciences (NIEHS) of the National Institutes of Health [grant numbers U01ES027272 and U24ES026946] as part of the Nanotechnology Health Implications Research (NHIR) Consortium; the Belgian American Educational Foundation Inc. Postdoctoral Fellowship to T.G.; the Eunice Kennedy Shriver National Institute of Child Health and Human Development of the National Institutes of Health [award number F31HD095594 to B.B.O]; the Organ Design and Engineering Postdoctoral Training (ODET) program through Brigham and Women's Hospital and the National Institute of Biomedical Imaging and Bioengineering of the National Institutes of Health [award number 5-T32-EB016652-04 to J.F.Z.]; and the American Chemical Society the Irving S. Sigal Postdoctoral Fellowship to H.A.M.A.

AUTHOR CONTRIBUTIONS

K.K.P. supervised the research. K.K.P., B.B.O. and T.G. designed the study. B.B.O. and T.G. performed the experiments, analyzed data and wrote the manuscript. J.F.Z. developed structural analysis macros and assisted in data analysis. H.A.M.A. assisted in substrate and nanoparticle preparation and conducted nanoparticle exposure experiments. J.A.J. assisted in cell culture and substrate preparation. D.B. and P.D. characterized nanoparticle preparations. All authors discussed the results and contributed to the writing of the manuscript.

ACKNOWLEDGMENTS

This work was made possible by access to the microfabrication facilities of the Center for Nanoscale Systems (CNS) at Harvard University, a member of the National Nanotechnology Infrastructure Network [award number 1541959], as well as the Harvard Materials Research and Engineering Center [award number DMR-1420570]. The ENMs used in the research presented in this publication have been procured or synthesized and characterized by the ERCC at the Center for Nanotechnology and Nanotoxicology at Harvard School of Public Health, part of the NIEHS/NHIR consortium. The content presented is solely the responsibility of the authors and does not necessarily represent the official views of the National Institutes of Health.

REFERENCES

1. Carmen-Orozco RP, Dávila-Villacorta DG, Cauna Y et al. Blood-brain barrier disruption and angiogenesis in a rat model for neurocysticercosis. *J Neurosci Res* 2019;**97**:137–48.
2. Kebir H, Kreymborg K, Ifergan I et al. Human TH17 lymphocytes promote blood-brain barrier disruption and central nervous system inflammation. *Nat Med* 2007;**13**:1173–5.
3. Menge T, Zhao Y, Zhao J et al. Mesenchymal stem cells regulate blood-brain barrier integrity through TIMP3 release after traumatic brain injury. *Sci Transl Med* 2012;**4**:161ra150.
4. Alford PW, Dabiri BE, Goss JA et al. Blast-induced phenotypic switching in cerebral vasospasm. *Proc Natl Acad Sci U S A* 2011;**108**:12705–10.
5. Ujiie M, Dickstein DL, Carlow DA et al. Blood–brain barrier permeability precedes senile plaque formation in an Alzheimer disease model. *Microcirculation* 2003;**10**:463–70.
6. Marco S, Skaper SD. Amyloid β-peptide1–42 alters tight junction protein distribution and expression in brain microvessel endothelial cells. *Neurosci Lett* 2006;**401**:219–24.
7. Saraiva C, Praça C, Ferreira R et al. Nanoparticle-mediated brain drug delivery: overcoming blood–brain barrier to treat neurodegenerative diseases. *J Control Release* 2016;**235**:34–47.
8. Zhou Y, Peng Z. Seven ES, Leblanc RM. Crossing the blood-brain barrier with nanoparticles. *J Control Release* 2018;**270**:290–303.
9. Sohal IS, O'Fallon KS, Gaines P et al. Ingested engineered nanomaterials: state of science in nanotoxicity testing and future research needs. *Part Fibre Toxicol* 2018;**15**:29. https://doi.org/10.1186/s12989-018-0265-1
10. Demokritou P, Gass S, Pyrgiotakis G et al. An in vivo and in vitro toxicological characterisation of realistic nanoscale CeO2 inhalation exposures. *Nanotoxicology* 2013;**7**:1338–50.
11. Sotiriou GA, Diaz E, Long MS et al. A novel platform for pulmonary and cardiovascular toxicological characterization of inhaled engineered nanomaterials. *Nanotoxicology* 2012;**6**:680–90.
12. Tsuda A, Donaghey TC, Konduru NV et al. Age-dependent translocation of gold nanoparticles across the air–blood barrier. *ACS Nano* 2019;**13**:10095–102.
13. Sharma HS, Hussain S, Schlager J et al. Influence of nanoparticles on blood–brain barrier permeability and brain edema formation in rats. *Acta Neurochir Suppl* 2010;**106**:359–64.
14. Maoz BM, Herland A, FitzGerald EA et al. A linked organ-on-chip model of the human neurovascular unit reveals the metabolic coupling of endothelial and neuronal cells. *Nat Biotechnol* 2018;**36**:865–74.
15. Booth R, Kim H. Characterization of a microfluidic in vitro model of the blood-brain barrier (μBBB). *Lab Chip* 2012;**12**:1784.
16. Herland A, van der AD, FitzGerald EA et al. Distinct contributions of astrocytes and pericytes to neuroinflammation identified in a 3D human blood-brain barrier on a chip. *PLoS One* 2016;**11**:e0150360.
17. Alford PW, Nesmith AP, Seywerd JN et al. Vascular smooth muscle contractility depends on cell shape. *Integr Biol* 2011;**3**:1063.
18. Wevers NR, Kasi DG, Gray T et al. A perfused human blood-brain barrier on-a-chip for high-throughput assessment of barrier function and antibody transport. *Fluids Barriers CNS* 2018;**23**:15. https://doi.org/10.1186/s12987-018-0108-3
19. Kirkton RD, Badie N, Bursac N. Spatial profiles of electrical mismatch determine vulnerability to conduction failure across a host-donor cell interface. *Circ Arrhythm Electrophysiol* 2013;**6**:1200–7.
20. Pasqualini FS, Agarwal A, O'Connor BB et al. Traction force microscopy of engineered cardiac tissues. *PLoS One* 2018;**13**:e0194706. https://doi.org/10.1371/journal.pone.0194706
21. Pedrotty DM, Klinger RY, Badie N et al. Structural coupling of cardiomyocytes and noncardiomyocytes: Quantitative comparisons using a novel micropatterned cell pair assay. *AJP Hear Circ Physiol* 2008;**295**:H390–400.
22. Huang S, Brangwynne CP, Parker KK et al. Symmetry-breaking in mammalian cell cohort migration during tissue pattern formation: role of random-walk persistence. *Cell Motil Cytoskeleton* 2005;**61**:201–13.
23. McCain ML, Lee H, Aratyn-Schaus Y et al. Cooperative coupling of cell-matrix and cell-cell adhesions in cardiac muscle. *Proc Natl Acad Sci U S A* 2012;**109**:9881–6.
24. Liu Z, Tan JL, Cohen DM et al. Mechanical tugging force regulates the size of cell-cell junctions. *Proc Natl Acad Sci U S A* 2010;**107**:9944–9.
25. Eweje F, Ardoña HAM, Zimmerman JF et al. Quantifying the effects of engineered nanomaterials on endothelial cell architecture and vascular barrier integrity using a cell pair model. *Nanoscale* 2019;**11**:17878–93.
26. Tietz S, Engelhardt B. Brain barriers: crosstalk between complex tight junctions and adherens junctions. *J Cell Biol* 2015;**209**:493–506.
27. Chen CS, Mrksich M, Huang S et al. Geometric control of cell life and death. *Science* 1997;**276**:1425–8.
28. Brookes NH. Riding the cell jamming boundary: geometry, topology, and phase of human corneal endothelium. *Exp Eye Res* 2018;**172**:171–80.
29. Yao L, Romero MJ, Toque HA et al. The role of RhoA/rho kinase pathway in endothelial dysfunction. *J Cardiovasc Dis Res* 2010;**1**:165–70.

30. Fukuhara S, Sakurai A, Sano H et al. Cyclic AMP potentiates vascular endothelial cadherin-mediated cell-cell contact to enhance endothelial barrier function through an Epac-Rap1 signaling pathway. *Mol Cell Biol* 2005;**25**:136–46.
31. Versaevel M, Grevesse T, Gabriele S. Spatial coordination between cell and nuclear shape within micropatterned endothelial cells. *Nat Commun* 2012;**3**:671.
32. Dejana E, Orsenigo F, Lampugnani MG et al. The role of adherens junctions and VE-cadherin in the control of vascular permeability. *J Cell Sci* 2008;**121**:2115–22.
33. Gavard J. Endothelial permeability and VE-cadherin. *Cell Adhes Migr* 2014;**25**:158–64.
34. Abu Taha A, Schnittler H-J. Dynamics between actin and the VE-cadherin/catenin complex: novel aspects of the ARP2/3 complex in regulation of endothelial junctions. *Cell Adhes Migr* 2014;**8**:125–35.
35. Park J-A, Kim JH, Bi D et al. Unjamming and cell shape in the asthmatic airway epithelium. *Nat Mater* 2015;**14**:1040–8.
36. Bi D, Lopez JH, Schwarz JM et al. A density-independent rigidity transition in biological tissues. *Nat Phys* 2015; **11**:1074–9.
37. Goeckeler ZM, Wysolmerski RB. Myosin light chain kinase-regulated endothelial cell contraction: The relationship between isometric tension, actin polymerization, and myosin phosphorylation. *J Cell Biol* 1995;**130**:613–27.
38. Adamson P, Etienne S, Couraud P-O et al. Lymphocyte migration through brain endothelial cell monolayers involves signaling through endothelial ICAM-1 via a rho-eependent pathway. *J Immunol* 1999;**162**:2964–73.
39. Stamatovic SM, Dimitrijevic OB, Keep RF et al. Protein kinase Calpha-RhoA cross-talk in CCL2-induced alterations in brain endothelial permeability. *J Biol Chem* 2006;**281**: 8379–88.
40. Totsukawa G, Wu Y, Sasaki Y et al. Distinct roles of MLCK and ROCK in the regulation of membrane protrusions and focal adhesion dynamics during cell migration of fibroblasts. *J Cell Biol* 2004;**164**:427–39.
41. Nel AE, Mädler L, Velegol D et al. Understanding biophysicochemical interactions at the nano–bio interface. *Nat Mater* 2009;**8**:543–57.
42. Zimmerman JF, Ardoña HAM, Pyrgiotakis G et al. Scatter enhanced phase contrast microscopy for discriminating mechanisms of active nanoparticle transport in living cells. *Nano Lett* 2019;**19**:793–804.
43. Beltran-Huarac J, Zhang Z, Pyrgiotakis G et al. Development of reference metal and metal oxide engineered nanomaterials for nanotoxicology research using high throughput and precision flame spray synthesis approaches. *NanoImpact* 2018;**10**:26–37.
44. Naz S, Beach J, Heckert B et al. Cerium oxide nanoparticles: a 'radical' approach to neurodegenerative disease treatment. *Nanomedicine* 2017;**12**:545–53.
45. Kumar V, Sharma N, Maitra SS. In vitro and in vivo toxicity assessment of nanoparticles. *Int Nano Lett* 2017;**7**: 243–56.
46. Bahadar H, Maqbool F, Niaz K et al. Toxicity of nanoparticles and an overview of current experimental models. *Iran Biomed J* 2016;**20**:1–11.
47. AshaRani PV, Low Kah Mun G, Hande MP et al. Cytotoxicity and genotoxicity of silver nanoparticles in human cells. *ACS Nano* 2009;**3**:279–90.
48. Dalle-Donne I, Rossi R, Giustarini D et al. Methionine oxidation as a major cause of the functional impairment of oxidized actin. *Free Radic Biol Med* 2002;**32**:927–37.
49. Emmert MY, Wolint P, Jakab A et al. Safety and efficacy of cardiopoietic stem cells in the treatment of post-infarction left-ventricular dysfunction – from cardioprotection to functional repair in a translational pig infarction model. *Biomaterials* 2017;**122**:48–62.
50. Chantre CO, Campbell PH, Golecki HM et al. Production-scale fibronectin nanofibers promote wound closure and tissue repair in a dermal mouse model. *Biomaterials* 2018;**166**:96–108.
51. Ahn S, Ardoña HAM, Campbell PH et al. Alfalfa nanofibers for dermal wound healing. *ACS Appl Mater Interfaces* 2019;**11**:33535–47.
52. Maniotis AJ, Chen CS, Ingber DE. Demonstration of mechanical connections between integrins, cytoskeletal filaments, and nucleoplasm that stabilize nuclear structure. *Proc Natl Acad Sci U S A* 1997;**94**:849–54.
53. Lee H, Adams WJ, Alford PW et al. Cytoskeletal prestress regulates nuclear shape and stiffness in cardiac myocytes. *Exp Biol Med* 2015;**240**:1543–54.
54. Aratyn-Schaus Y, Pasqualini FS, Yuan H et al. Coupling primary and stem cell–derived cardiomyocytes in an in vitro model of cardiac cell therapy. *J Cell Biol* 2016;**212**: 389–97.
55. Freese C, Anspach L, Deller RC et al. Gold nanoparticle interactions with endothelial cells cultured under physiological conditions. *Biomater Sci* 2017;**5**:707–17.
56. Liu Y, Rogel N, Harada K et al. Nanoparticle size-specific actin rearrangement and barrier dysfunction of endothelial cells. *Nanotoxicology* 2017;**11**:846–56.
57. Setyawati MI, Tay CY, Chia SL et al. Titanium dioxide nanomaterials cause endothelial cell leakiness by disrupting the homophilic interaction of VE–cadherin. *Nat Commun* 2013;**4**:1673.
58. Heckman KL, DeCoteau W, Estevez A et al. Custom cerium oxide nanoparticles protect against a free radical mediated autoimmune degenerative disease in the brain. *ACS Nano* 2013;**7**:10582–96.
59. Grevesse T, Versaevel M, Circelli G et al. A simple route to functionalize polyacrylamide hydrogels for the independent tuning of mechanotransduction cues. *Lab Chip* 2013; **13**:777.
60. Bray M-A, Sheehy SP, Parker KK. Sarcomere alignment is regulated by myocyte shape. *Cell Motil Cytoskeleton* 2008;**65**:641–51.
61. Butler JP, Tolić-Nørrelykke IM, Fabry B et al. Traction fields, moments, and strain energy that cells exert on their surroundings. *Am J Physiol Physiol* 2002;**282**: C595–605.
62. Ye GJC, Aratyn-Schaus Y, Nesmith AP et al. The contractile strength of vascular smooth muscle myocytes is shape dependent. *Integr Biol* 2014;**6**:152–63.
63. Dong J, Carpinone PL, Pyrgiotakis G et al. Synthesis of precision gold nanoparticles using Turkevich method. *KONA Powder Part J* 2020:1–19.
64. Demokritou P, Bchel R, Molina RM et al. Development and characterization of a versatile engineered nanomaterial generation system (VENGES) suitable for toxicological studies. *Inhal Toxicol* 2010;**22**:107–16.
65. DeLoid GM, Cohen JM, Pyrgiotakis G et al. Preparation, characterization, and in vitro dosimetry of dispersed, engineered nanomaterials. *Nat Protoc* 2017;**12**:355–71.
66. DeLoid GM, Cohen JM, Pyrgiotakis G et al. Advanced computational modeling for in vitro nanomaterial dosimetry. *Part Fibre Toxicol* 2015;**12**:32.

67. DeLoid G, Cohen JM, Darrah T et al. Estimating the effective density of engineered nanomaterials for in vitro dosimetry. *Nat Commun* 2014;**5**:3514.
68. Taurozzi JS, Hackley VA, Wiesner MR. Ultrasonic dispersion of nanoparticles for environmental, health and safety assessment–issues and recommendations. *Nanotoxicology* 2011;**5**:711–29.
69. Cohen J, DeLoid G, Pyrgiotakis G et al. Interactions of engineered nanomaterials in physiological media and implications for in vitro dosimetry. *Nanotoxicology* 2013;**7**:417–31.